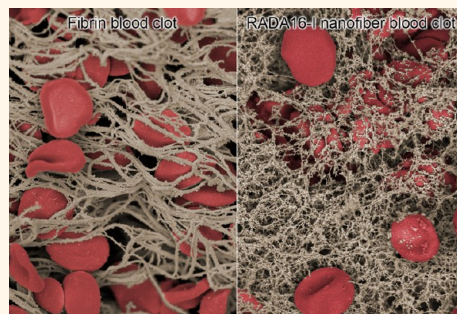


Clotting Mimicry from Robust Hemostatic Bandages Based on Self-Assembling Peptides

Bryan B. Hsu,^{†,‡,||} William Conway,[§] Cory M. Tschabrunn,[▽] Manav Mehta,[#] Monica B. Perez-Cuevas,[⊗] Shuguang Zhang,[○] and Paula T. Hammond^{*,‡,§,||}

[†]Departments of Chemistry, [‡]Chemical Engineering, and [§]Physics, Massachusetts Institute of Technology, Cambridge, Massachusetts 02139, United States, [○]Koch Institute for Integrative Cancer Research, Massachusetts Institute of Technology, Cambridge, Massachusetts 02139, United States, ^{||}Institute for Soldier Nanotechnologies, Cambridge, Massachusetts 02139, United States, [▽]Harvard-Thorndike Electrophysiology Institute, Beth Israel Deaconess Medical Center Harvard Medical School, Boston, Massachusetts 02215, United States, [#]3-D Matrix Medical Technology, Waltham, Massachusetts 02451, United States, [⊗]School of Chemical & Biomolecular Engineering, Georgia Institute of Technology, Atlanta, Georgia 30332, United States, and [○]Center for Bits & Atoms, Massachusetts Institute of Technology, Cambridge, Massachusetts 02139, United States

ABSTRACT Uncontrolled bleeding from traumatic wounds is a major factor in deaths resulting from military conflict, accidents, disasters and crime. Self-assembling peptide nanofibers have shown superior hemostatic activity, and herein, we elucidate their mechanism by visualizing the formation of nanofiber-based clots that aggregate blood components with a similar morphology to fibrin-based clots. Furthermore, to enhance its direct application to a wound, we developed layer-by-layer assembled thin film coatings onto common materials used for wound dressings—gauze and gelatin sponges. We find these nanofibers elute upon hydration under physiological conditions and generate nanofiber-based clots with blood. After exposure to a range of harsh temperature conditions (-80 to 60 °C) for a week and even 5 months at 60 °C, these hemostatic bandages remain capable of releasing active nanofibers. In addition, the application of these nanofiber-based films from gauze bandages was found to accelerate hemostasis in porcine skin wounds as compared to plain gauze. The thermal robustness, in combination with the self-assembling peptide's potent hemostatic activity, biocompatibility, biodegradability, and low cost of production, makes this a promising approach for a cheap yet effective hemostatic bandage.



KEYWORDS: bleeding · nanofibers · hemorrhage · blood clots · wound dressings

Blood loss is one of the greatest causes of mortality as more than 85% of deaths from potentially survivable wounds are due to exsanguinating hemorrhage during military combat¹ with significance in civilian trauma as well.² The development of explosive weaponry over the last ~150 years has seen a transition from ballistics (e.g., gunshots) to explosives (e.g., improvised explosive devices, mortars, rocket-propelled grenades and landmines) as the predominant mechanism of injury³ with the latter increasing the odds of large traumatic wounds in multiple areas. Traumatic wounds can frequently lead to coagulopathy, where clotting is impaired due to systemically reduced blood flow resulting in anticoagulation and enhanced degradation of fibrin, a main constituent of clots.⁴ This was found to occur in a quarter of civilian trauma patients⁵

and more than a third of military casualties,⁶ with their likelihood correlated with the severity of injury.^{5,6} As a consequence, coagulopathy resulted in a 4-fold greater civilian mortality⁵ and 6-fold greater military mortality.⁶ With the increasing prevalence of large traumatic injury, it is critical to develop a hemostatic dressing capable of facilitating blood clotting through a mechanism independent of the body's own coagulation system so that hemostasis may be achieved despite coagulopathy.⁷

Although several topical hemostats have been developed in the recent past,⁸ few portable and rapidly deployable hemostatic systems can meet the demands of use in military and emergency care situations, especially in developing nations. The instability, cost, preparation time, and/or bulk of typical hemostats limits their portability

* Address correspondence to Hammond@mit.edu.

Received for review April 20, 2015 and accepted August 18, 2015.

Published online August 18, 2015
10.1021/acsnano.5b02374

© 2015 American Chemical Society

and use in challenging situations, such as disasters and combat. For such uncontrolled conditions, it is desirable to have a dry hemostat material that is active despite long-term storage at extreme temperatures (*i.e.*, between -10 and 55 °C), is simple to apply, inexpensive, easy to manufacture on an industrial scale, biodegradable, and has no undesirable side effects (*e.g.*, burns or thrombosis).^{9,10} Although some hemostatic dressings such as those based on chitosan (Celox and Hemcon bandages), smectite (WoundStat), and kaolin (Combat Gauze) have shown improvement in establishing hemostasis, they remain deficient in a number of desired criteria¹¹ and multiple revisions have not resulted in significant improvement suggesting that the potential of these technologies may have already been maximized.^{12,13}

An alternative approach to establishing hemostasis is through the use of hydrogels composed of biodegradable self-assembling peptides. In solution, these peptides form nanofibers that can rapidly coagulate blood,¹⁴ but their hydration state precludes their deployment in the field. As the vast majority of mass is composed of water, this introduces undue bulk as well as exposes the peptides to degradation if subjected to elevated temperature.¹⁵ Alternatively, films of these nanofibers deposited on to absorbent bandage materials would provide a lightweight, uncomplicated, and immediately functional means of applying the peptide in a concentrated dry form. This would help overcome some challenges presented by severely bleeding wounds that can dilute materials before reaching the site of injury, or extreme environmental conditions (*e.g.*, wind and precipitation) that can make application of powders or solutions challenging.

Herein, we aimed to create an advanced hemostatic dressing based on a clotting strategy that is independent of the body's coagulation mechanisms and can coat common bandaging materials. We first clarify the uncertainty surrounding the mechanism behind how self-assembling peptides, namely RADA16-I, rapidly coagulate blood by showing the three-dimensional nanofiber morphology when in contact with whole blood in the hydrated state. Second, we transform the self-assembling hydrogel into a dry film formulation using a Layer-by-Layer (LbL) assembly technique that allows for mechanically stable conformal coatings through nondenaturing electrostatic interactions. These films are composed of RADA16-I and biodegradable polysaccharides, which were coated onto the relevant bandaging materials of gauze and absorbent gelatin sponges. We find that when incorporated into LbL films, RADA16-I retains its nanofiber morphology and remains capable of forming nanofiber-based clots. We also find that these nanofibers eluted from films coating gauze remain active after exposure to extreme temperatures (-80 to 60 °C) and as long as five months at the extreme temperature of 60 °C. Furthermore, they

are shown to accelerate hemostasis in a porcine skin wound model.

RESULTS AND DISCUSSION

Nanofiber Clotting Mechanism. The ability for self-assembling peptides to rapidly coagulate blood has been hypothesized to occur through nanofiber entanglements that entrap blood components.¹⁶ We chose to examine this effect using RADA16-I, which is one of the more well-studied self-assembling peptides^{17–19} and has previously been examined as a hydrogel hemostat.^{20,21} To elucidate this effect and its possible implications on RADA16-I for thin film assembly and biomedical application, we studied the morphological characteristics of the solution-phase nanofibers by scanning electron microscopy (SEM). For SEM examination of the hydrated structures, the materials in solution were chemically fixed using glutaraldehyde, then serially dehydrated in ethanol, and critically point dried with CO₂ after which they were sputter-coated with ~ 8 nm of Au/Pd. We found that RADA16-I in PBS, pH 7.4 (Figure 1A) forms a dense network of highly entangled nanofibers that is morphologically consistent with previous observations by SEM^{22,23} and atomic force microscopy.¹⁷ Examination at higher magnification reveals the individual nanofibers to be highly interpenetrated with nanoscale pores (Figure 1A, *inset*) that are consistent with its macroscopic formation of a hydrogel.¹⁷ Separate characterization of EDTA anticoagulated whole blood reveals the presence of red blood cells (RBCs) and platelets with the absence of fibrin clot formation (Figure 1B). To examine the mechanisms of hemostasis of RADA16-I in a wound, we recapitulated this scenario *ex vivo* by combining RADA16-I with anticoagulated whole blood, and found that the interwoven nanofibers visibly entrapped blood components (Figure 1C). Interestingly, this nanofiber-based clot appears to have morphological similarities with a fibrin clot, in which the blood components are physically trapped by polymerized fibrin stalks during the natural coagulation process (Figure 1D). Although this effect has been the proposed mechanism of hemostasis with histology²⁴ and AFM²⁰ providing circumstantial evidence, these SEM images directly demonstrate the physical entanglement of blood components with RADA16-I to form a nanofiber-based clot. Because the formation of these nanofiber clots occurs under anticoagulating conditions, RADA16-I may provide significant hemostatic activity even under coagulopathic conditions.

Numerous topical approaches can facilitate hemostasis by activating or enhancing the body's natural coagulation mechanisms to accelerate fibrin clot formation. Hemostatic dressings based on biomacromolecules and proteins like chitosan and fibrinogen or inorganic nanomaterials like kaolin and smectite are capable of facilitating fibrin clot formation, but each suffers from

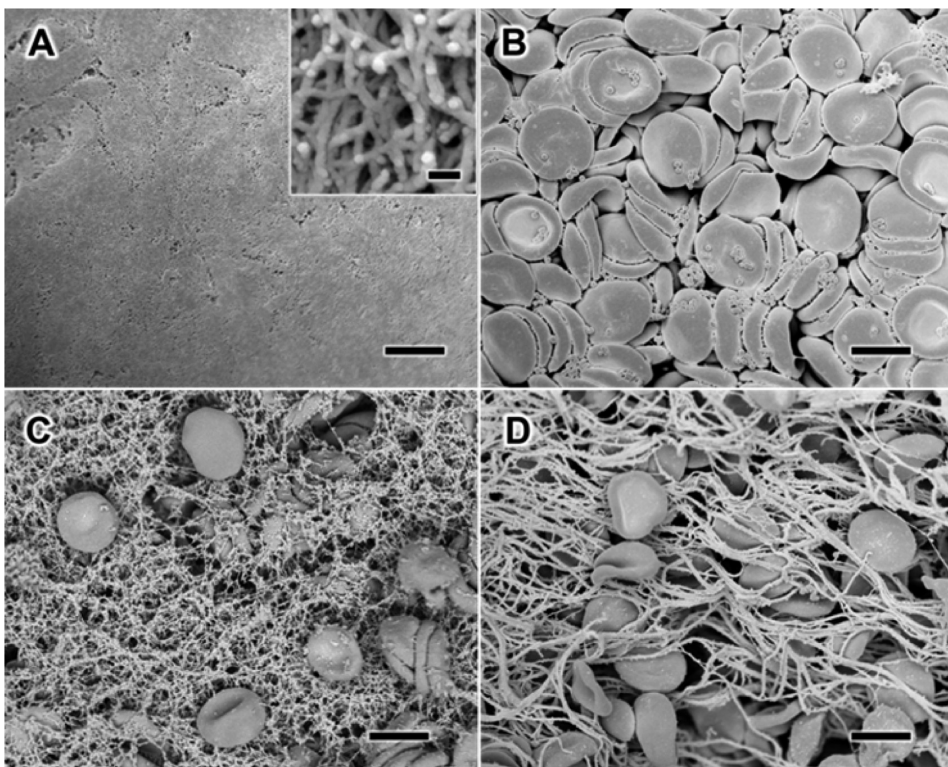


Figure 1. Scanning electron microscopy (SEM) visualization of the morphology of the interaction between whole blood and RADA16-I. When alone in solution, RADA16-I spontaneously self-assembles into interpenetrating nanofibers (A), while anticoagulated whole blood shows the presence of red blood cells and platelets without fibrin formation (B). Mixture of RADA16-I with anticoagulated whole blood reveals the physical entrapment of blood components in a network of peptide nanofibers (C), which appears similar to naturally coagulating fibrin-based clots (D). Scale bars represent 5 μm (A–D) and 100 nm (A, inset).

some drawbacks including limited effectiveness, difficulty to apply formulations (*e.g.*, viscous gel or powder), exothermic reactions on contact with blood, and non-biodegradability that requires debridement after use,⁹ while hemostasis generated by nanofiber clots based on the RADA16-I self-assembling peptide has also been shown to be rapid,²¹ and its biodegradability, biocompatibility, low cost, and thermal stability make it an interesting alternative strategy. It is critical for these nanofibers to directly reach the site of injury, which we aim to achieve by coating them onto common bandaging materials in a concentrated dry film-based formulation.

Multilayer Film Assembly. We developed a thin-film coating using an all-aqueous layer-by-layer (LbL) assembly approach that has shown the versatility to coat a variety of materials with tunable loading and release properties. In developing a bilayer (RADA16-I/polyanion)_n film architecture, we examined biocompatible and naturally derived polyanions like hyaluronic acid (HA, 2 MDa and 500 kDa), chondroitin sulfate (CS), and dextran sulfate (DS), as shown in Figure 2. These films were assembled by dip-LbL under acidic conditions ($\text{pH} \sim 2$) to facilitate ionic and hydrogen bonding interactions between the polysaccharides and RADA16-I (Figure 2). At this pH,¹⁵ the latter's aspartic

acid and arginine side chains are neutral and cationic, respectively. In LbL film assembly, tuning extrinsic conditions such as pH or ionic strength can induce two components to form multilayer films when they attain complementary functionality (*i.e.*, cationic/anionic or H-bond donor/H-bond acceptor).²⁵ After deposition and dehydration, the film's subsequent exposure to physiological conditions (PBS, pH 7.4) markedly changes the nature of the pH-sensitive intermolecular interactions and the increased negative charge density due to deprotonation of the acid groups initiates film disassembly and nanofiber release.

We screened through these polyanionic film components using the dip-LbL technique and compared their resultant properties. Out of the four polyanions examined, DS and HA (2 MDa) yielded films with the best RADA16-I loadings and comparable thicknesses (Figure S1), which can result from a number of factors including charge density,^{26,27} secondary interactions,^{27–29} and molecular weight.³⁰ We had examined the effect a periodic drying step (*i.e.*, standing to allow for evaporation or intermittent drying with compressed air) had on films containing RADA16-I and found that this increased the resultant film thicknesses (Figure S2). Therefore, we included a drying step in the film assembly of all films, as described in the Materials and Methods.

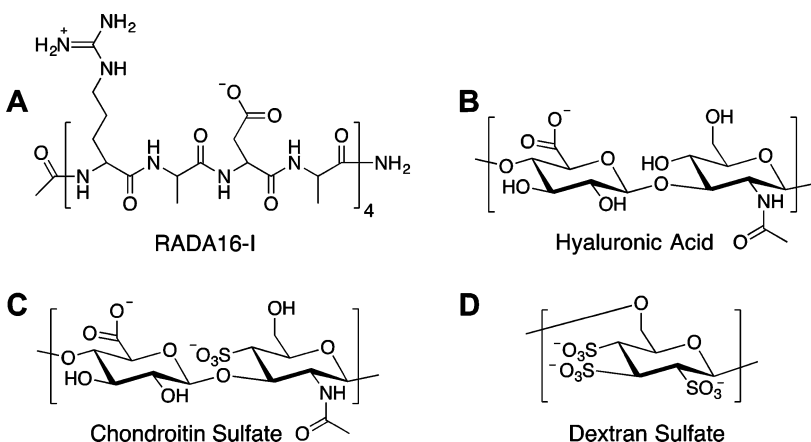


Figure 2. Chemical structures of components used in LbL film assembly. The 16-amino acid self-assembling peptide, RADA16-I, consists of a Arg-Ala-Asp-Ala motif repeated four times (A). Hyaluronic acid (B), chondroitin sulfate (C), and dextran sulfate (D) are biopolymers with negative charge at physiological pH and are used as components in film construction.

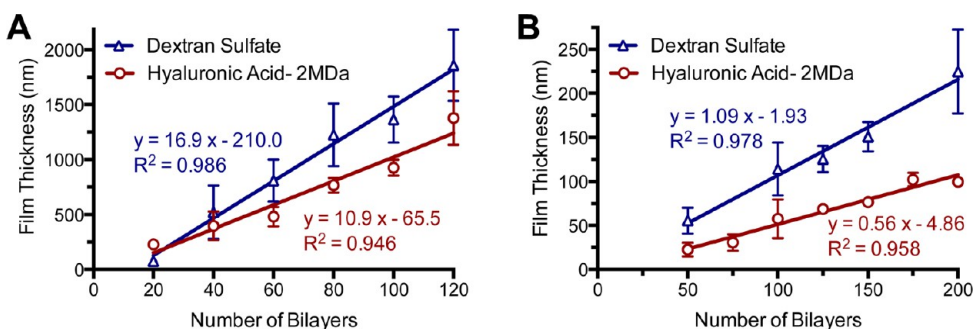


Figure 3. Film growth of LbL assembled films. Film growth of (RADA16-I/hyaluronic acid) ($n = 6$) and (RADA16-I/dextran sulfate) ($n = 6$) films assembled by dip LbL show a proportional growth of total film thickness with increasing numbers of bilayers deposited (A). This film growth concomitant with number of bilayers deposited was similarly observed with films assembled by spray LbL (B).

The introduction of drying does not negatively affect LbL film growth,³¹ and can sometimes promote multilayer assembly when it may otherwise be difficult^{32,33} by increasing the amount of material deposited per layer through film reorganization of more hydrophobic components near the surface.^{34,35} We found that drying, in conjunction with incubation steps of 30 min, significantly improved the film assembly. By linear regression of the growth curves for DS and HA based films, we found that 16.9 and 10.9 nm were deposited per bilayer, respectively (Figure 3A), consistent with an approximate monolayer of the nanofibers, which have diameters of ~5–10 nm.

In addition to using dip-LbL, we examined spray-LbL assembly in which the substrate was coated by exposure to a preprogrammed sequence of aerosolized solutions rather than being immersed in these solutions. This technique is more amenable for coating porous and absorbent materials and film assembly is finished in a fraction of the time that would typically be required for dip LbL.^{36,37} Examinations of these same architectures constructed by spray-LbL onto solid materials (glass slides) yielded much thinner films with 1.09 and 0.56 nm per bilayer for the DS and HA-based films,

respectively (Figure 3B). This submonolayer deposition of nanofibers and polyelectrolyte per bilayer is likely due to a combination of the 10-fold lower concentrations of RADA16-I and polyanion used during assembly and the significantly shorter deposition times associated with spray-LbL assembly, which exploits kinetic trapping for adsorption³⁷ rather than approaching equilibrium as is the case for dip-LbL assembly. By aerosolizing these materials in a predefined sequence, films can be rapidly assembled within hours onto a variety of possible substrates with uniquely tunable properties³⁶ and invites its potential scalable fabrication for continuous high throughput manufacturing.³⁸ In both cases of dip- and spray-LbL, we found linear growth behavior, which is typically indicative of minimal interdiffusion occurring during film assembly. With the growth characteristics being quite similar, we continued our examination of spray-LbL films because of its greater translational potential. Furthermore, we chose to examine 200-bilayer films because the RADA16-I loading was sufficient for additional characterization and these films could be constructed in a reasonable amount of time (~3 h).

The tunable nature of LbL film assembly enables the possibility of adjusting certain factors to optimize

desirable characteristics. For example, increasing the RADA16-I loading per area is likely to positively influence hemostasis, as higher peptide concentrations to an extent have shown shorter times to hemostasis when applied as a gel.¹⁴ This may be achieved with thicker films, which can be assembled with more concentrated solutions, prolonged deposition times, and increased number of layers. Increasing the loading density (*i.e.*, mass fraction of RADA16-I in the film) is also an option and may be improved with a judicious choice of polyanion or aqueous conditions (*e.g.*, ionic strength or pH of solution). Other options, such as use

of dip-LbL, can result in different film thicknesses and RADA16-I mass fractions, but becomes more challenging due to longer film assembly times or the use of porous/absorbent materials.

Film Characteristics. The spray LbL assembled films showed interesting surface morphologies, which differed between DS and HA polyanions. We examined three substrates, a glass slide (Figure 4A), cotton gauze (Figure 4D), and a gelatin sponge (Figure 4G). On flat surfaces, $(\text{RADA16-I/DS})_{200}$ films have a rough appearance (Figure 4B) with the distinct outlines of randomly overlapping nanofibers that are more clearly

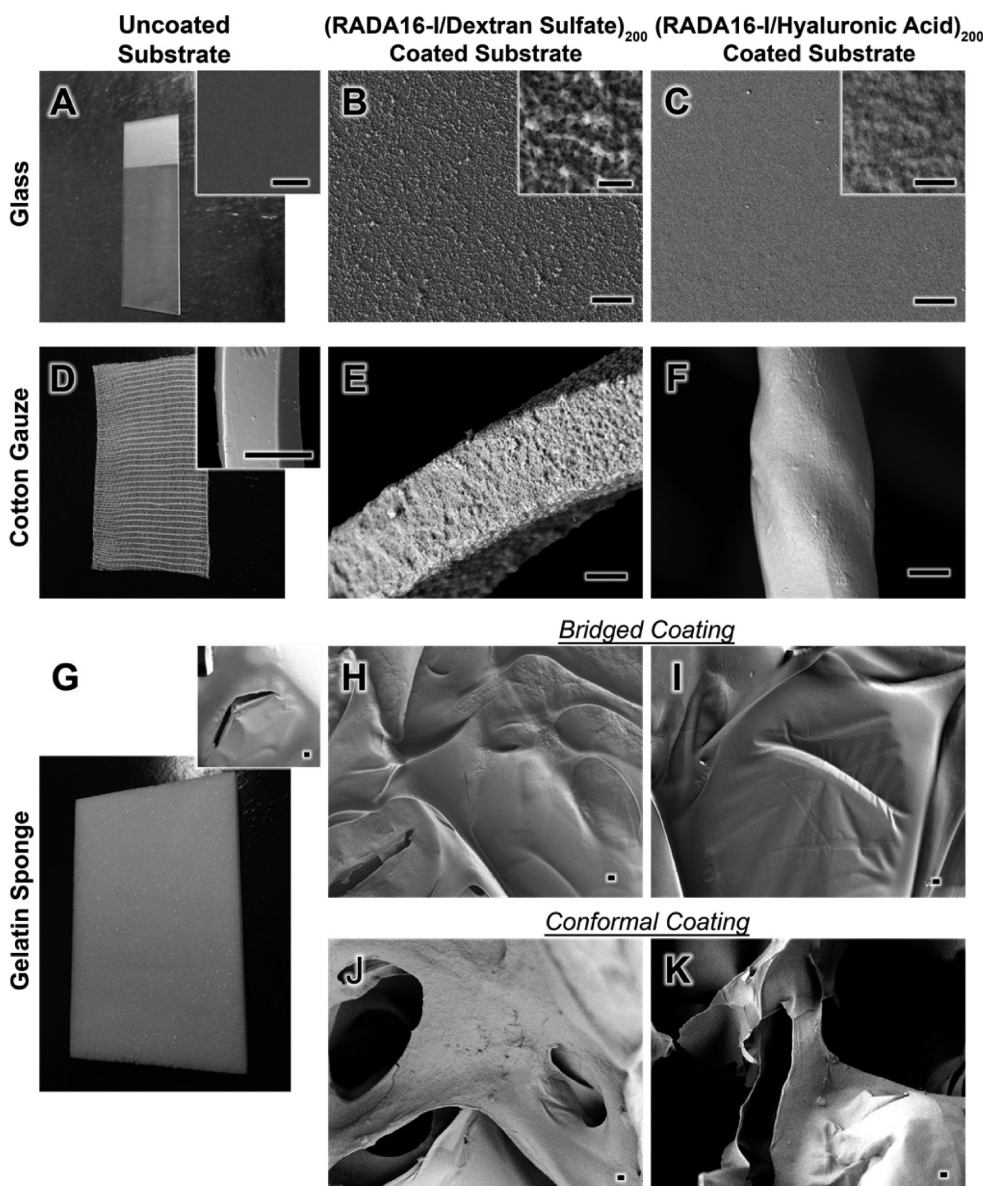


Figure 4. Surface morphology of films deposited by spray-LbL onto substrates of glass, cotton gauze, and gelatin sponge. SEM was used to capture the surface morphologies of the uncoated glass (A, inset) and cotton gauze (D, inset) and gelatin sponge (G, inset), as well as those substrates coated with $(\text{RADA16-I/DS})_{200}$ films (B, E, H, and J) and $(\text{RADA16-I/HA})_{200}$ films (C, F, I, and K). The films deposited onto glass show the characteristic outlines of nanofibers (B and C), which can be similarly observed to a lesser degree when deposited onto cotton gauze (E and F). Both films can also be deposited onto gelatin sponges in bridged (H and I) and conformal (J and K) coatings showing that a diversity of substrates, even highly absorbent biodegradable gelatin, can be coated with this approach. Scale bars represent 5 μm (B, C, E, F, H, I, J, K, and insets of D and G) and 500 nm (A–C, insets).

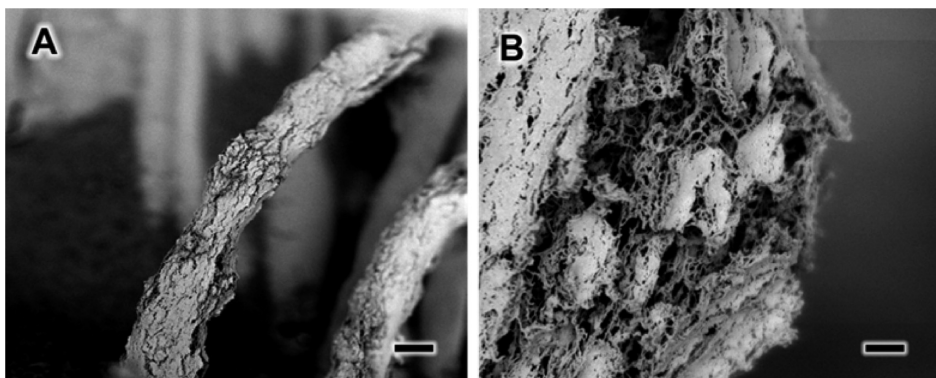


Figure 5. Visualization of partially hydrated $(\text{RADA16-I/DS})_{200}$ films deposited onto cotton gauze by spray LbL. After film assembly, they are dried for storage and ready for application. Their exposure to humidified air allows for the visualization of the film's morphology during partial hydration (A). Closer examination of the film at higher resolution shows the presence of intact nanofibers within the film, indicating they are readily available in these LbL assembled films (B). Scale bars represent $10 \mu\text{m}$ (A) and $1 \mu\text{m}$ (B).

distinguishable at higher magnification (Figure 4B, inset). For $(\text{RADA16-I/HA})_{200}$ similarly deposited onto glass (Figure 4C), the films have a much smoother texture with higher magnification also showing the outlines of nanofibers, though less obvious (Figure 4C, inset). The less apparent nanofiber structures may be a characteristic of a denser and/or thicker adsorbed HA layer that fills the voids between layered nanofibers; a lower charge density yielding loopier and denser chain conformations due to decreased charge repulsion between chain segments may generate more filled-in monolayers. When depositing these films onto cotton gauze, (Figure 4E,F) and onto gelatin sponges in bridged (Figure 4H,I) and conformal (Figure 4J,K) coatings, the film morphologies were clearly transferred as evidenced by the distinctly different surface textures as compared to plain (uncoated) substrates (Figure 4A,D, G and Figure S3). We discovered that during assembly of these films onto the gelatin sponges, the air-drying we used after each layer caused films to bridge across the pores. We believe this may be occurring when aerosolized droplets initially absorb onto the surface of the gelatin sponges, briefly spanning the pores on the surface. When applying a gentle air drying, it causes the solution to rapidly evaporate, leaving some of the nanofibers bridged across the pores before they have the opportunity to directly interact completely with the surface of the gelatin. This forms a thin film across the pores, onto which subsequent layers are deposited to create this bridged coating (Figure 4H,I). We found that by omitting the air-drying step (*i.e.*, instead, allowing the film to stand for the same duration), the resultant films conformally coated the intricate geometry of the gelatin sponges (Figure 4J,K). In this case, the aerosolized solutions were able to deposit onto the surface and absorb into the bacterial, transporting the film components directly to the surface of the sponge. We have observed a similar tunability in electrospun mats where vacuum applied to the back of these nonabsorbent,

porous material could create a conformal coating by pulling the deposited solutions through the substrate, whereas the absence of vacuum resulted in films only forming on the surface.³⁶

Under the acidic pH conditions we used to facilitate film assembly, it has been shown that nanofibers readily assemble.¹⁵ When aiming to generate rapid hemostasis on-contact, it is imperative that the film be immediately capable of forming a nanofiber-based clot, and examinations of the dry films (Figure 4) suggest that the RADA16-I is indeed incorporated in fibrillar form. For additional insight into RADA16-I's supramolecular structure within the film, we studied the morphology of $(\text{RADA16-I/DS})_{200}$ films on gauze after partial hydration provided by exposure to a humidifier, which was followed by chemical cross-linking with glutaraldehyde, serial dehydration, and critical point drying to preserve the structure. SEM examination reveals that this film is fractured and swollen (Figure 5A), which can be expected as RADA16-I typically forms a hydrogel in solution. Higher magnification of the interior of the film shows that it is composed of highly entangled and interwoven nanofibers that are clearly discernible (Figure 5B) indicating that RADA16-I is indeed incorporated into the film as nanofibers. Because the supramolecular structure is a critical component to generating hemostasis, its film incorporation as already-assembled nanofibers potentially improves the film's response time.

To confirm that LbL assembly with a polyanion could generate superior coatings over other basic deposition approaches, we also examined the surface morphologies of gauze coated by a spray-LbL architecture of $(\text{RADA16-I/nothing})_{200}$, where "nothing" was the aqueous solution without polyanion (Figure S4A,B) and by immersion in a 0.1 mg/mL solution of RADA16-I (the same concentration used for spray-LbL) (Figure S4C,D). Examination of their surfaces revealed little deposition of RADA16-I with some small regions coated, but large swaths of areas bare. Quantification of RADA16-I

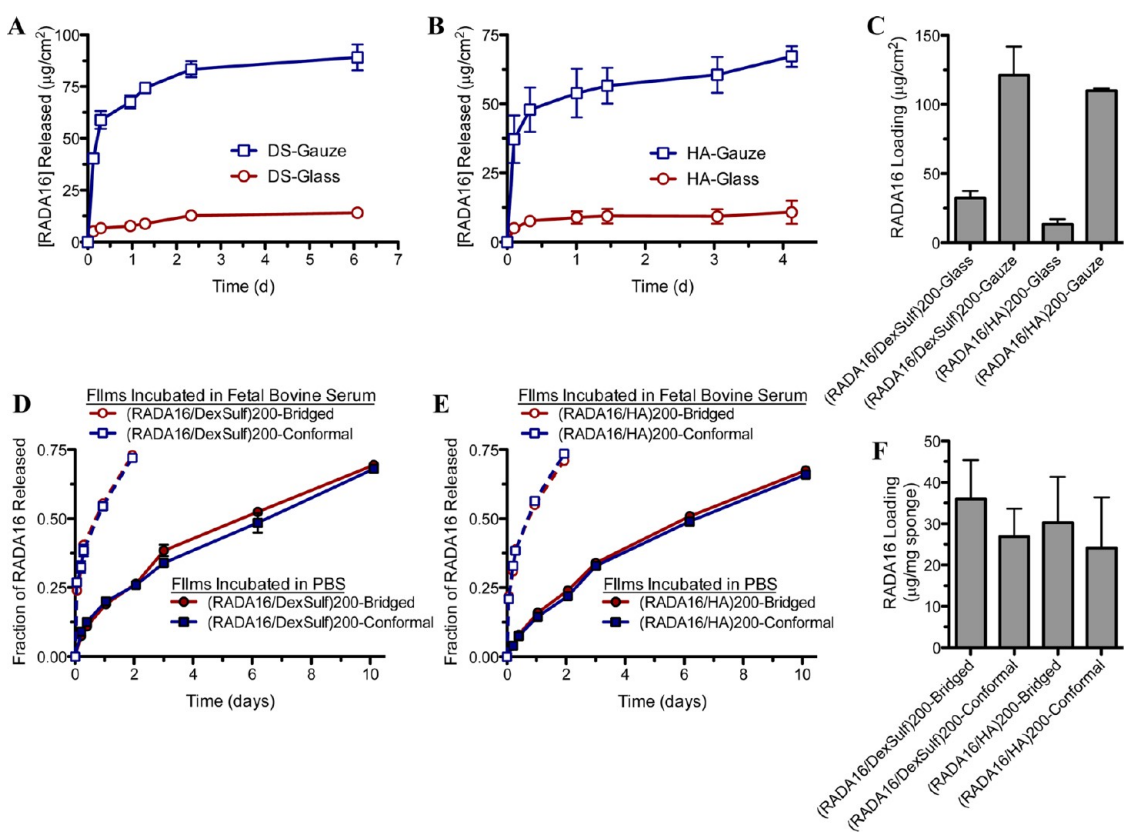


Figure 6. Loading and release characteristics of RADA16-I from spray-LbL assembled films. Incubation in PBS, pH 7.4 at 37 °C reveals that RADA16-I is eluted into solution from films of (RADA16-I/dextran sulfate)₂₀₀ (A and D) and (RADA16-I/hyaluronic acid)₂₀₀ (B and E) deposited onto glass and gauze (A and B) and gelatin sponges (D and E). When films are eluted into more complex medium, fetal bovine serum, RADA16-I is released more rapidly into solution due to greater disruption of the film. Coating a higher surface area substrate such as gauze as compared to a flat glass shows higher loadings of RADA16-I (C), while bridged and conformal coatings of gelatin sponges were less dissimilar (F) ($n = 4$).

showed relatively low loadings of 5.0 ± 1.3 and $4.0 \pm 1.0 \mu\text{g}/\text{cm}^2$ for these two films, respectively.

Nanofiber Release and Functionality. For insight into how these films based on the hemostatic self-assembling peptide would respond to full hydration, we studied the RADA16-I release behavior into the physiological conditions of PBS, pH 7.4 at 37 °C and quantified their overall loadings in spray-LbL films deposited onto glass, gauze, and gelatin sponges. For (RADA16-I/DS)₂₀₀ films (Figure 6A) and (RADA16-I/HA)₂₀₀ films (Figure 6B) on glass and gauze, the peptides release rapidly within the first half-day with substantial amounts of peptide loaded into the film (Figure 6C); similar release profiles were observed with dip-LbL films (Figure S1B). Comparatively, when these films are deposited onto gelatin sponges, both DS-based films (Figure 6D) and HA-based films (Figure 6E) show a more sustained release with substantial RADA16-I loadings (Figure 6F). We suspected there may be stronger intrinsic interaction between the films and the gelatin substrate through additional intermolecular interactions (e.g., hydrogen bonding) and when compounded with the absorptive nature of the biodegradable foam, may allow for greater entanglement and more intrinsic association between the film and the substrate. By assembling these films

under acidic conditions (pH ~ 2), the pH-sensitive hydrogen-bonding and electrostatic interactions that were established during assembly are disrupted in a PBS, pH 7.4 solution and hence the charge imbalance facilitates film disassembly. Ideally, the release would be immediate, but our observation suggests some additional factors are able to slow RADA16-I release, which may be due to the high degree of entanglement of the nanofibers when dried in a film, as well as some remaining weak intermolecular interactions. As we found with other hydrogen-bonded films, immersion in blood facilitated film disassembly when PBS did not, which is likely due to proteins displacing the intermolecular interactions of the film.³⁹ With our own films of (RADA16-I/DS)₂₀₀ (Figure 6D) and (RADA16-I/HA)₂₀₀ (Figure 6E) deposited onto gelatin sponges, we similarly found significantly accelerated release when fetal bovine serum (FBS) was used as opposed to PBS.

Although the release of peptide into solution is likely beneficial to hemostasis, its response when in direct physical contact with blood at the site of injury is the most critical determinant to its success. For example, a nanofiber clot not only generates a mechanical plug to stop additional bleeding, but also aggregates and concentrates blood components (e.g., platelets

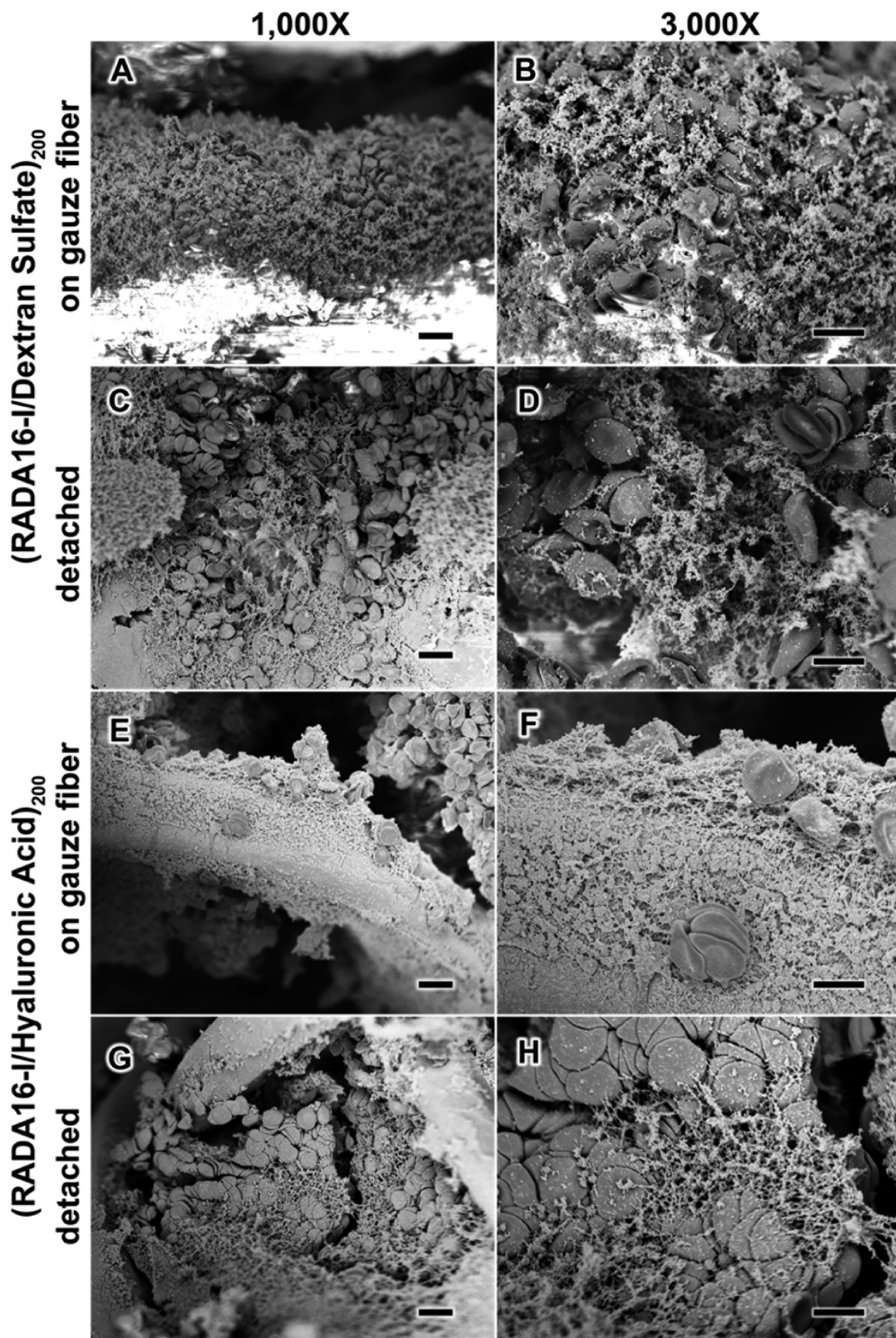


Figure 7. Surface characterization of anticoagulated whole blood upon contact with spray LbL assembled films. SEM characterization of (RADA16-I/DS)₂₀₀ films (A–D) and (RADA16/HA)₂₀₀ films (E–H) in contact with anticoagulated whole blood shows that the blood components interact with the films both on the gauze fibers (A, B, E, and F) and detached (C, D, G, and H). Scale bars represent 10 μm (A, C, E, and G) and 5 μm (B, D, F, and H).

and RBCs) to further enhance the coagulative response.^{40,41} Therefore, to gain greater insight into how these nanofiber-based films would respond to a wound, we studied the morphology of gauze coated with (RADA16-I/DS)₂₀₀ films (Figure 7A–D) and (RADA16-I/HA)₂₀₀ films (Figure 7E–H), upon

contact with anticoagulated whole human blood. These films showed that nanofiber clotting was capable of occurring both on the gauze fibers (Figure 7A,B,E,F) as well as in the films detached from the gauze (Figure 7C, D,G,H), and in each of these cases, the morphological appearances resemble what we observed for a simple

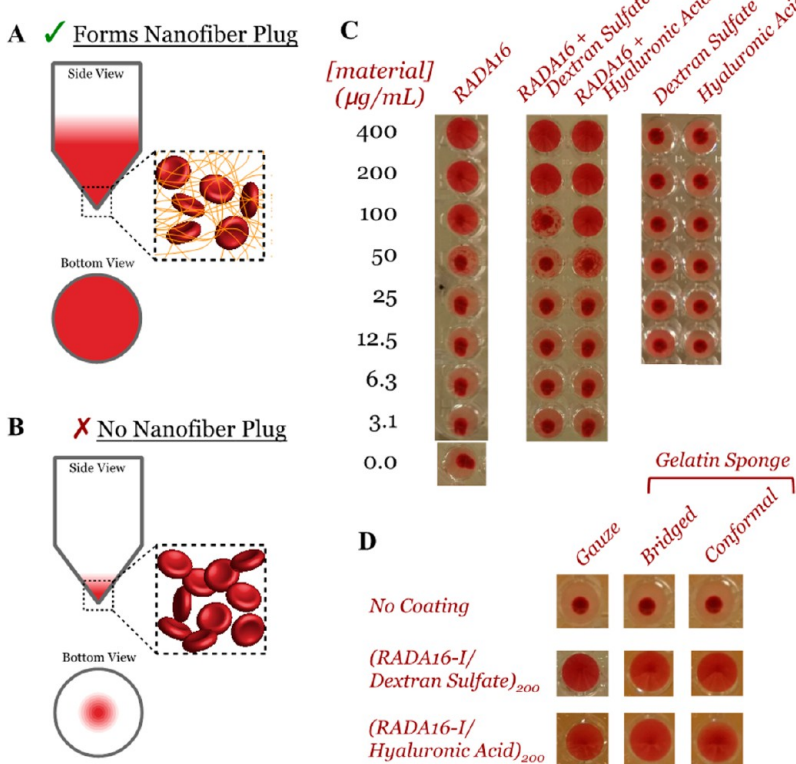


Figure 8. *In vitro* determination of nanofiber formation of RADA16-I and its ability to form nanofiber clots with red blood cells (RBCs). The premise of this assay is represented schematically where the presence of nanofiber-forming RADA16-I can interact with RBCs to maintain their suspension in solution (A), whereas their absence or inability for nanofiber formation results in RBC settling to the bottom (B). Standard dilutions of various controls reveal there is a necessary concentration of RADA16-I for this effect, the polymers used during film assembly (*i.e.*, dextran sulfate and hyaluronic acid) are not inhibitory, and these polymers alone are not capable of forming these nanofiber clots (C). The RADA16-I eluted from these films remains capable of generating these nanofiber clots with RBCs (D).

mixture of RADA16-I with anticoagulated whole blood (Figure 1C). These studies show that RADA16-I remains capable of forming a nanofiber-clot in blood with the nanofibers forming an entangled and interpenetrated network that can entrap and aggregate blood components on contact.

In addition to the microscopic morphological examination of these films with blood, we utilized an *in vitro* test for nanofiber formation of film components released into PBS by adopting a suspension assay that had previously been correlated to *in vivo* hemostatic activity.¹⁶ We mixed PBS solutions with rabbit RBCs in a 96-well microtiter plate with V-shaped wells and allowed the RBCs to settle. For solutions containing sufficient concentrations of nanofibers, their entanglement with the RBCs keeps them in suspension, and thus, a view from underneath shows red in the well's entirety (Figure 8A). For insufficient concentrations, the RBCs settle to the bottom of the wells to form a small red area in the center when viewed from underneath (Figure 8B). We used this approach to examine serial dilutions of RADA16-I alone, in equal concentration mixtures with DS or HA, and with DS or HA alone (Figure 8C). These results show that we can indeed titrate the loading of nanofibers to entrap RBCs in

solution, and that the polyanions did not have significant impact on this effect, nor could the polyanions entrap RBCs on their own. Examination of the activity of film-components released into solution from gauze and gelatin sponge substrates showed they retained the ability to maintain RBCs in suspension while uncoated substrates had no activity (Figure 8D). This in effect supports our observations for blood interacting with films deposited onto gauze (Figure 7) and, in a more rapid approach, indicates the nanofibers released into solution from films deposited onto gelatin sponges in bridged and conformal coatings are also capable of forming nanofiber-based clots with RBCs.

One distinct feature of using these nanofibers as hemostatic agents, in addition to being nontoxic and composed of biodegradable peptides, is their ability to continue to self-assemble despite exposure to harsh environmental conditions such as pH or temperature that would denature and inactivate other biologic hemostats. Exposure of nanofiber solutions to elevated temperatures as high as 80 °C was found to disrupt the ionic and hydrogen bonding present in the supramolecular aggregates, but nanofibers were reformed after returning to room temperature.¹⁸ To demonstrate the robustness of these films, we incubated (RADA16-I/DS)₂₀₀

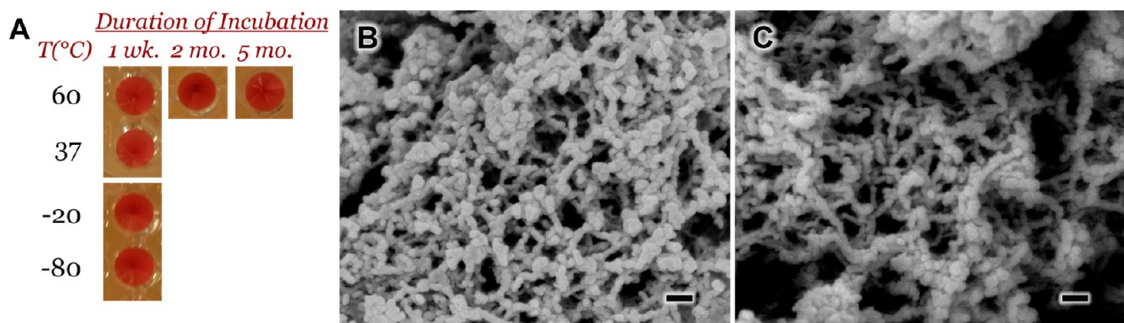


Figure 9. Effect of extreme temperature conditions on the clotting activity of RADA16-I eluted from spray-LbL films. Films of $(\text{RADA16-I/DS})_{200}$ were deposited on gauze and incubated in desiccant at temperatures ranging from -80 to $+60$ $^{\circ}\text{C}$ for different time periods. Upon elution into solution, the nanofibers were found to retain their *in vitro* activity by clot formation with RBCs (A). The RADA16-I eluted from films incubated at 60 $^{\circ}\text{C}$ for 2 months (B) and 5 months (C) were found to retain their ability to form interwoven nanofibers. Scale bars represent 100 nm.

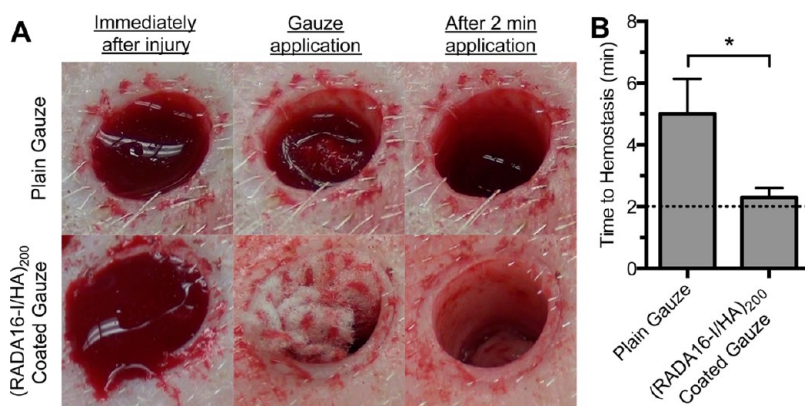


Figure 10. Application of plain gauze and $(\text{RADA16-I/HA})_{200}$ coated gauze in a porcine skin puncture injury. Representative images of gauze samples applied to bleeding injuries show that the RADA16-I based coating has increased efficacy in achieving hemostasis within an initial 2 min time period over plain gauze (A). Measuring the time to achieving hemostasis at 2 min application intervals showed that the $(\text{RADA16-I/HA})_{200}$ coating ($n = 7$) significantly accelerates hemostasis as compared to plain gauze ($n = 6$). $*p < 0.05$.

coated gauze at -80 , -20 , 37 , and 60 $^{\circ}\text{C}$ for 1 week in desiccant and found that the nanofibers released into solution retained their activity when mixed with RBCs (Figure 9A). Furthermore, films incubated at 60 $^{\circ}\text{C}$ for 2 and 5 months still released active nanofibers (Figure 9A) and closer examination showed that the released peptide could still form the interwoven and entangled nanofibers (Figure 9B,C). With the extremes of world temperatures, the stability of these films at elevated temperatures for extended periods bodes well for the possibility of its use in bandages without the need of the cold-chain that is commonly necessary for preserving the activity of biologics.

Thus far, we have found substantial *in vitro* evidence of hemostatic activity. For the potential translation of this technology into clinical application, an understanding of its activity *in vivo* is imperative. Therefore, we applied these films to porcine skin puncture wounds to elucidate their ability to accelerate hemostasis. After an 8 mm diameter biopsy and three scalpel incisions to induce significant bleeding, we applied plain gauze or $(\text{RADA16-I/HA})_{200}$ coated gauze for 2 min and then removed it to determine its

effect on hemostasis (Figure 10A). If bleeding continued, a fresh piece of plain or coated gauze was applied for another 2 min with the process repeated for up to 8 min (*i.e.*, four applications). To assess the severity of bleeding, injuries were scored (blinded to the sample) on a scale of 0 through 4, constituting a range from no bleeding to severe bleeding (Table S1). On the basis of this metric, we only included wounds scoring 2 or greater immediately after injury and found no difference between control and treatment groups (3.0 ± 0.4 and 2.9 ± 0.3 , respectively). As a result of gauze application, we found a significant reduction in the time needed for hemostasis (*i.e.*, a bleeding score of 0) when using $(\text{RADA16-I/HA})_{200}$ coated gauze as opposed to plain gauze (Figure 10B). The RADA16-I film generated hemostasis within the first 2 min incubation period in nearly all cases, suggesting that bleeding may have stopped in less than 2 min. In contrast, plain gauze required nearly 5 min (two to three applications) to stop bleeding (Figure 10B).

Our construction and assembly of RADA16-I from dry thin films supported on gauze improves its portability and enables application directly to the wound

but requires contact with blood for activation, which should be taken into account when comparing their effects on bleeding. Treatment with RADA16-I as an aqueous gel has been generally reported to accelerate coagulation; hemostasis was achieved in 6 s in a rat skin injury compared to 75 s for an untreated wound,¹⁴ 10 s in a rat liver injury compared to 204 s when treated with saline,¹⁴ and 10 s in a rat liver injury compared to 90 s with PBS.⁴² By comparison, chitosan, a muco-adhesive polymer with hemostatic properties that also act independently to the host coagulation mechanisms, accelerated coagulation of blood *in vitro* from 5 to 2 min as a gel.⁴³ One report indicated chitosan gel was able to reduce bleeding times in rabbit tongue incision wounds from 368 to 209 s,⁴⁴ while another report using chitosan gel in a rat femoral vein injury found no improved hemostasis compared to saline.⁴⁵ Bandages based on chitosan have been reported to be effective *in vivo*.¹¹ For example, when applied to severe porcine liver injuries, five of eight animals reached hemostasis within 4 min compared to none of the seven animals that received plain gauze.⁴⁶ With the different animal models and metrics for hemostasis reported in the literature, it will be important in future studies to directly compare the performance of these RADA16-I based bandages to other advanced hemostatic materials in aggressive large animal models.

CONCLUSIONS

Generating rapid hemostasis from a lightweight, flexible, and easily applied device or bandage is highly desirable for improving survival from wounding caused by armed conflict, crime, accidents, or disasters. Utilizing a hemostatic approach that is independent of the body's coagulation mechanism would be tremendously

advantageous over traditional bandages that are ineffective in instances of coagulopathy. Self-assembling peptides, especially RADA16-I, have demonstrated to be highly effective in generating hemostasis *in vivo* when applied as a solution. Morphological examination of the interaction between these nanofibers and anticoagulated whole blood shows the formation of a nano-fiber-based clot that entraps the blood components in a similar fashion to fibrin-based clots. By incorporation into LbL assembled (RADA16-I/DS)_n and (RADA16-I/HA)_n films, we were able to utilize common bandage and wound dressing materials and found nanofiber clots could be generated on contact with blood. These films were also thermally robust against denaturation from a range of temperatures and could release active nanofibers even after 5 months at 60 °C. Application of (RADA16-I/HA)₂₀₀ coated gauze in porcine skin wounds showed that these films are able to accelerate hemostasis *in vivo* and demonstrates a promising approach to creating a cheap, biodegradable, biocompatible, and robust hemostatic bandage. By introducing such features that overcome the challenges of cost and shelf life commonly faced by other advanced hemostatic bandages, these RADA16-I based LbL films are an encouraging step forward for the development of an affordable consumer-level bandage.

Additional studies will be critical to elaborating on the translatability of these bandages. Herein, we demonstrate their potential, but a comprehensive kinetic study of clinical coagulation parameters (e.g., prothrombin time and partial thromboplastin time) in conjunction with large animal models of aggressively bleeding wounds such as near-fatal coagulopathic porcine wound models would be important for determining their feasibility in such situations.

MATERIALS AND METHODS

Unless otherwise noted, all materials were obtained from Sigma-Aldrich and used without further purification. Hyaluronic acid (HA, $M_w = 2$ MDa and 500 kDa) was obtained from Lifecore Biomedical, chondroitin sulfate sodium salt (CS, $M_w = 85$ kDa) from TCI International, and dextran sulfate sodium salt (DS, $M_w = 500$ kDa) from Calbiochem. Glutaraldehyde (Grade I 25%) and collagenase (Type I) were purchased from Sigma-Aldrich. Human whole blood (EDTA anticoagulated) was obtained from Hemacare, and washed and pooled 10% rabbit red blood cells (RBCs) were obtained from Lampire Biological Laboratories. Solutions of 1% (10 mg/mL) RADA16-I were a generous donation from 3DMatrix. Fluorescently labeled RADA16-I (RADA16-I^{FAM}) was functionalized by 5-carboxyfluorescein at the N-terminus through a -Gly-Gly- linker and synthesized by the MIT Biopolymers Laboratory. Gelatin sponges were a generous donation from Ferrosan.

LbL Film Assembly. Substrates of silicon wafers or glass microscope slides were precleaned with methanol, acetone, and water prior to plasma irradiation (Harrick PDC-32G) for at least 1 min and immersion in RADA16-I solution (1 mg/mL in 10 mM HCl for dip-LbL and 0.1 mg/mL in 10 mM HCl for spray-LbL) for at least 15 min before additional film assembly. Cotton gauze was prepared by ~30 s of plasma irradiation and then immersed in 0.1 mg/mL in 10 mM HCl prior to spray-LbL assembly. Gelatin

sponges were used as received without additional preparation. Films were allowed to stand dry for 60 min after every 10 bilayers.

Dip LbL films of (RADA16-I/polyanion)_n were assembled onto silicon (prepared as described above) by sequential immersion into 1 mg/mL RADA16-I in 10 mM HCl (30 min), rinsing in 10 mM HCl (10, 20, and 30 s), immersion into 1 mg/mL polyanion (30 min), and rinsing in 10 mM HCl (10, 20, and 30 s), which constituted one bilayer and was repeated for *n*-bilayers.

Spray LbL films of (RADA16-I/polyanion)_n were assembled onto glass, cotton gauze, and gelatin (prepared as described above). For the latter two, house vacuum was applied behind the substrates to facilitate more thorough film coatings. Solutions were aerosolized at 15 PSI at 0.25 mL/s flow rates using an automated film assembly instrument (Svaya). Bilayer films were constructed by spraying substrates in the following sequence: 0.1 mg/mL RADA16-I in 10 mM HCl (2 s), waiting period (5 s), wash with 10 mM HCl (3 s), air-drying (8 s), 0.1 mg/mL polyanion in 10 mM HCl (2 s), waiting period (5 s), wash with 10 mM HCl (3 s), and air-drying (8 s). This constituted one bilayer and was repeated for *n*-bilayers. For gelatin sponges, the use of air-drying generated a bridged film conformation, while its replacement with a waiting period generated conformal coatings.

Film Characterization. Thicknesses of films deposited onto flat substrates (silicon or glass) were determined by measuring the

step-height difference between the film and a razor-scored region (Dektak 150 Profilometer).

Release profiles of films deposited onto silicon, glass, and gauze were quantified by immersion in 500 μL of PBS, pH 7.4 at 37 °C and periodic replacement with fresh aliquots of PBS prewarmed to 37 °C. The collected aliquots were analyzed for their RADA16-I content using a bicinchoninic acid (BCA) assay (Thermo Scientific) according to the manufacturer's instructions with incubation of the reagent and sample for 30 min at 60 °C to enhance sensitivity. Under these conditions, we saw no background signal from the polyanions used in this study. This BCA assay was capable of distinguishing RADA16-I released from all substrates, except the gelatin sponges, which released protein that obscured measurement. For quantification of the RADA16-I released from these samples, films were assembled with a RADA16-I solution containing a 1:20 fraction of RADA16-I^{FAM}, and peptide release was studied by incubating in 1 mL of PBS or FBS at 37 °C and periodically sampling 300 μL for analysis and replacing it with fresh prewarmed solution. The collected aliquots were measured for fluorescence ($\lambda_{\text{ex}} = 480 \text{ nm}$; $\lambda_{\text{em}} = 525 \text{ nm}$) and RADA16-I was quantified by comparison to a standard curve.

Total RADA16-I loadings on glass, silicon and gauze were determined by complete dissolution of the films in 225 μL of 0.1 M NaOH at 37 °C for ~2 h, after which the solution was quenched with 225 μL of 0.1 M HCl and the addition of 50 μL of 10× PBS (for a final 1× concentration) to stabilize the pH. The RADA16-I content was measured by a BCA assay, similarly to as described earlier. Because the gelatin sponges introduced difficulties in completely eluting RADA16-I from the films, the substrate was digested using collagenase prior to fluorescence quantification. To the 1 mL of PBS or FBS containing film deposited onto gelatin sponges were added 100 μL of 10 mg/mL collagenase and 50 mM CaCl₂ in PBS prior to incubation at 37 °C for ~4 h followed by fluorescence quantification.

Nanofiber Activity *In Vitro*. The ability for RADA16-I to form a nanofiber-based clot *in vitro* was determined using a similar assay previously described.¹⁶ Solutions of 95 μL of PBS containing RADA16-I diluted from stocks or released from films were added to V-shaped 96-well microtiter plates followed by the addition of 10 μL of 10% rabbit RBCs. The wells were sealed with an optically clear adhesive film, agitated at ~900 rpm for 15 min, and then incubated at 4 °C for at least 4 h prior to examination.

Clotting Characterization. Fibrin clots were generated by adding 25 μL of 0.2 M CaCl₂ to 475 μL of anticoagulated whole blood and the mixture was gently rocked at room temperature for 30 min. To study the nanofiber interaction with blood, 1 μL of 1% RADA16-I was mixed with 9 μL of anticoagulated whole blood and the mixture was incubated at room temperature for ~5 min. Anticoagulated whole blood was studied without additional treatment and RADA16-I was studied at 0.1% in PBS, pH 7.4. For examination of blood's interaction with (RADA16-I-polyanion)₂₀₀ films, 5 μL of anticoagulated whole blood was deposited on top of film-coated gauze and the sample was incubated at room temperature for ~5 min with exposure to a humidifier to prevent drying out. All samples were chemically fixed, dehydrated, and critically point dried as described below.

Scanning Electron Microscopy. Biological samples were prepared on a 0.03 μm poly(ether sulfone) membrane filter (Stereitech) by fixation with 2.5% glutaraldehyde (diluted from 25%) in PBS for 4 h at room temperature, then serially dehydrated with 10 mL of H₂O (twice), 25% ethanol, 50% ethanol, 75% ethanol, 80% ethanol, 90% ethanol, and 100% ethanol (twice). Samples in ethanol were then critically point dried using CO₂ (Sorvall Critical Point Drying System). These dried biological samples and other samples already in dry form were sputter coated with ~8 nm of Au/Pd prior to examination using a field-emission SEM (JEOL 6700F). Dry LbL films were studied in LEI mode (10 kV and 8 mm working distance), while biological samples were studied in SEI mode (5.0 kV and ~6 mm working distance).

Porcine Skin Injury. The porcine skin injury was conducted in the Beth Israel Deaconess Medical Center experimental electrophysiology laboratory and conformed to the Position of the American Heart Association on Research Animal Use as well as

to the Declaration of Helsinki. The study was performed under an approved institutional animal care and use committee protocol. A male Yorkshire swine weighing 42 kg was pre-anesthetized with telazol (4.7 mg/kg IM), and then anesthetized with inhaled isoflurane during the procedure. The animal was intubated and ventilation was maintained between 10 and 14 breaths/min with tidal volumes between 300 and 500 mL. Hemodynamic assessment including core body temperature, heart rate, oxygen saturation, and blood pressure were continuously monitored. Therapeutic anticoagulation was maintained with intravenous heparin and was confirmed with serial activated clotting time testing between 250 and 350 s.

Wounds were generated by an 8 mm biopsy to the mid-dorsal region. After removal of biopsied tissue, three incisions 2 cm deep were made with a #10 scalpel at 60° rotations. The wound was allowed to bleed for approximately 5 s, during which the severity of bleeding was scored from 0 (no bleeding) through 4 (severe bleeding), as described in Table S1. Plain or (RADA16-I/HA)₂₀₀ coated gauze samples of 5 cm × 2 cm were rolled up and then inserted into the wound. After 2 min, the sample was removed and the severity of bleeding was scored. For wounds that continued to bleed, fresh pieces of gauze were applied for 2 min before removal and assessment. This was repeated for a maximum of four applications. Wounding and application of samples were done blinded to the type of gauze (i.e., plain or coated). Hemostasis was achieved when bleeding was given a score of 0. Statistical analysis was conducted with a one-tailed Wilcoxon rank sum test to ascertain the significance the (RADA16-I/HA)₂₀₀ coating had on reducing time to hemostasis compared to the plain gauze.

Conflict of Interest: The authors declare the following competing financial interest(s): M.M. is an employee of 3-D Matrix Medical Technology; S.Z. is a founder and director of 3-D Matrix Medical Technology.

Acknowledgment. The authors would like to thank W. Di-Natale for assistance with critical point drying, and R. Polak and J. McConville for their insight. The authors also wish to express their appreciation to the Institute for Soldier Nanotechnologies at MIT, supported by the Army Research Office and Army Research Laboratories, whose facilities and/or equipment were used to conduct the research reported in this paper. In addition, we thank the MIT Koch Institute Swanson Biotechnology Center, which is supported by the Koch Institute Core Grant P30-CA14051 from the NCI, for the use of facilities, and specifically the Biopolymers Laboratory. This research was supported by the U.S. Army Research Office under contract W911NF-13-D-0001 and the Air Force under contract W911NF-07-D-0004.

Supporting Information Available: The Supporting Information is available free of charge on the ACS Publications website at DOI: 10.1021/acsnano.5b02374.

Film thicknesses and RADA16-I loadings of dip-LbL assembled (RADA16-I-polyanion)₄₀ films; effect of intermittent drying on film thickness; SEM images of the surfaces of uncoated glass, gauze and gelatin substrates; surface morphology of gauze coated by non-LbL methods; the release of RADA16-I from dip-LbL assembled films; scoring criteria for the severity of bleeding (PDF)

REFERENCES AND NOTES

- Kelly, J. F.; Ritenour, A. E.; McLaughlin, D. F.; Bagg, K. A.; Apodaca, A. N.; Mallak, C. T.; Pearse, L.; Lawnick, M. M.; Champion, H. R.; Wade, C. E.; et al. Injury Severity and Causes of Death from Operation Iraqi Freedom and Operation Enduring Freedom: 2003–2004 Versus 2006. *J. Trauma* **2008**, 64, S21–S26.
- Evans, J. A.; van Wensem, K. J. P.; McDougall, D.; Lee, K. A.; Lyons, T.; Balogh, Z. J. Epidemiology of Traumatic Deaths: Comprehensive Population-Based Assessment. *World J. Surg.* **2010**, 34, 158–163.
- Belmont, P. J.; Schoenfeld, A. J.; Goodman, G. Epidemiology of Combat Wounds in Operation Iraqi Freedom and Operation Enduring Freedom: Orthopaedic Burden of Disease. *J. Surg. Orthop. Adv.* **2010**, 19, 2–7.

4. Brohi, K.; Cohen, M. J.; Ganter, M. T.; Schultz, M. J.; Levi, M.; Mackersie, R. C.; Pittet, J. F. Acute Coagulopathy of Trauma: Hypoperfusion Induces Systemic Anticoagulation and Hyperfibrinolysis. *J. Trauma* **2008**, *64*, 1211–7 discussion 1217.
5. Brohi, K.; Singh, J.; Heron, M.; Coats, T. Acute Traumatic Coagulopathy. *J. Trauma* **2003**, *54*, 1127–1130.
6. Niles, S. E.; McLaughlin, D. F.; Perkins, J. G.; Wade, C. E.; Li, Y.; Spinella, P. C.; Holcomb, J. B. Increased Mortality Associated with the Early Coagulopathy of Trauma in Combat Casualties. *J. Trauma* **2008**, *64*, 1459–63 discussion 1463–5.
7. Kheirabadi, B. Evaluation of Topical Hemostatic Agents for Combat Wound Treatment. *U.S. Army Med. Dep. J.* **2011**, *25*–37.
8. Achneck, H. E.; Sileshi, B.; Jamiolkowski, R. M.; Albala, D. M.; Shapiro, M. L.; Lawson, J. H. A Comprehensive Review of Topical Hemostatic Agents: Efficacy and Recommendations for Use. *Ann. Surg.* **2010**, *251*, 217–228.
9. Gordy, S. D.; Rhee, P.; Schreiber, M. A. Military Applications of Novel Hemostatic Devices. *Expert Rev. Med. Devices* **2011**, *8*, 41–47.
10. *Capturing the Full Power of Biomaterials for Military Medicine: Report of a Workshop*; The National Academies Press: Washington, D.C., 2004.
11. Bennett, B. L.; Littlejohn, L. F.; Kheirabadi, B. S.; Butler, F. K.; Kotwal, R. S.; Dubick, M. A.; Bailey, J. A. Management of External Hemorrhage in Tactical Combat Casualty Care: Chitosan-Based Hemostatic Gauze Dressings - Tccc Guidelines-Change 13–05. *J. Spec. Oper. Med.* **2014**, *14*, 40–57.
12. Rall, J. M.; Cox, J. M.; Songer, A. G.; Cestero, R. F.; Ross, J. D. Comparison of Novel Hemostatic Dressings with Quikclot Combat Gauze in a Standardized Swine Model of Uncontrolled Hemorrhage. *J. Trauma Acute Care Surg.* **2013**, *75*, S150–6.
13. Grissom, T. E.; Fang, R. Topical Hemostatic Agents and Dressings in the Prehospital Setting. *Curr. Opin. Anaesthesiol.* **2015**, *28*, 210–6.
14. Ellis-Behnke, R. At the Nanoscale: Nanohemostat, a New Class of Hemostatic Agent. *Wiley Interdiscip. Rev. Nanomed. Nanobiotechnol.* **2011**, *3*, 70–78.
15. Arosio, P.; Owczarz, M.; Wu, H.; Butté, A.; Morbidelli, M. End-to-End Self-Assembly of Rada 16-1 Nanofibrils in Aqueous Solutions. *Biophys. J.* **2012**, *102*, 1617–1626.
16. Luo, Z.; Wang, S.; Zhang, S. Fabrication of Self-Assembling D-Form Peptide Nanofiber Scaffold D-Eak16 for Rapid Hemostasis. *Biomaterials* **2011**, *32*, 2013–2020.
17. Yokoi, H.; Kinoshita, T.; Zhang, S. G. Dynamic Reassembly of Peptide Rada16 Nanofiber Scaffold. *Proc. Natl. Acad. Sci. U. S. A.* **2005**, *102*, 8414–8419.
18. Ye, Z.; Zhang, H.; Luo, H.; Wang, S.; Zhou, Q.; Du, X.; Tang, C.; Chen, L.; Liu, J.; Shi, Y.-K.; et al. Temperature and Ph Effects on Biophysical and Morphological Properties of Self-Assembling Peptide Rada16–1. *J. Pept. Sci.* **2008**, *14*, 152–162.
19. Cormier, A. R.; Ruiz-Orta, C.; Alamo, R. G.; Paravastu, A. K. Solid State Self-Assembly Mechanism of Rada16-1 Designer Peptide. *Biomacromolecules* **2012**, *13*, 1794–1804.
20. Wang, T.; Zhong, X.; Wang, S.; Lv, F.; Zhao, X. Molecular Mechanisms of Rada16–1 Peptide on Fast Stop Bleeding in Rat Models. *Int. J. Mol. Sci.* **2012**, *13*, 15279–15290.
21. Ellis-Behnke, R. G.; Liang, Y.-X.; Tay, D. K. C.; Kau, P. W. F.; Schneider, G. E.; Zhang, S.; Wu, W.; So, K.-F. Nano Hemostat Solution: Immediate Hemostasis at the Nanoscale. *Nanomedicine* **2006**, *2*, 207–15.
22. Gelain, F.; Horii, A.; Zhang, S. Designer Self-Assembling Peptide Scaffolds for 3-D Tissue Cell Cultures and Regenerative Medicine. *Macromol. Biosci.* **2007**, *7*, 544–551.
23. Ho, D.; Fitzgerald, M.; Bartlett, C. A.; Zdyrko, B.; Luzinov, I. A.; Dunlop, S. A.; Iyer, K. S. The Effects of Concentration-Dependent Morphology of Self-Assembling Rada16 Nanoscaffolds on Mixed Retinal Cultures. *Nanoscale* **2011**, *3*, 907–910.
24. Song, H.; Zhang, L.; Zhao, X. Hemostatic Efficacy of Biological Self-Assembling Peptide Nanofibers in a Rat Kidney Model. *Macromol. Biosci.* **2010**, *10*, 33–39.
25. Decher, G. Fuzzy Nanoassemblies: Toward Layered Polymeric Multicomposites. *Science* **1997**, *277*, 1232–1237.
26. Shiratori, S. S.; Rubner, M. F. Ph-Dependent Thickness Behavior of Sequentially Adsorbed Layers of Weak Polyelectrolytes. *Macromolecules* **2000**, *33*, 4213–4219.
27. Xu, L.; Ankner, J. F.; Sukhishvili, S. A. Steric Effects in Ionic Pairing and Polyelectrolyte Interdiffusion within Multi-layered Films: A Neutron Reflectometry Study. *Macromolecules* **2011**, *44*, 6518–6524.
28. Clark, S. L.; Hammond, P. T. The Role of Secondary Interactions in Selective Electrostatic Multilayer Deposition. *Langmuir* **2000**, *16*, 10206–10214.
29. Gilbert, J. B.; Rubner, M. F.; Cohen, R. E. Depth-Profilin X-Ray Photoelectron Spectroscopy (Xps) Analysis of Interlayer Diffusion in Polyelectrolyte Multilayers. *Proc. Natl. Acad. Sci. U. S. A.* **2013**, *110*, 6651–6656.
30. Sui, Z.; Salloum, D.; Schlenoff, J. B. Effect of Molecular Weight on the Construction of Polyelectrolyte Multilayers: Stripping Versus Sticking. *Langmuir* **2003**, *19*, 2491–2495.
31. Halthur, T. J.; Claesson, P. M.; Elofsson, U. M. Stability of Polypeptide Multilayers as Studied by *in Situ* Ellipsometry: Effects of Drying and Post-Buildup Changes in Temperature and Ph. *J. Am. Chem. Soc.* **2004**, *126*, 17009–17015.
32. Raposo, M.; Pontes, R. S.; Mattoso, L. H. C.; Oliveira, O. N. Kinetics of Adsorption of Poly(O-Methoxyaniline) Self-Assembled Films. *Macromolecules* **1997**, *30*, 6095–6101.
33. Wang, L.; Wang, L.; Su, Z. Surface Defects in Polyelectrolyte Multilayers: Effects of Drying and Deposition Cycle. *Soft Matter* **2011**, *7*, 4851–4855.
34. Decher, G.; Lvov, Y.; Schmitt, J. Proof of Multilayer Structural Organization in Self-Assembled Polycation Polyanion Molecular Films. *Thin Solid Films* **1994**, *244*, 772–777.
35. Lvov, Y.; Ariga, K.; Onda, M.; Ichinose, I.; Kunitake, T. A Careful Examination of the Adsorption Step in the Alterate Layer-by-Layer Assembly of Linear Polyanion and Polycation. *Colloids Surf., A* **1999**, *146*, 337–346.
36. Krogman, K. C.; Lowery, J. L.; Zacharia, N. S.; Rutledge, G. C.; Hammond, P. T. Spraying Asymmetry into Functional Membranes Layer-by-Layer. *Nat. Mater.* **2009**, *8*, 512–518.
37. Krogman, K. C.; Zacharia, N. S.; Schroeder, S.; Hammond, P. T. Automated Process for Improved Uniformity and Versatility of Layer-by-Layer Deposition. *Langmuir* **2007**, *23*, 3137–3141.
38. Krogman, K. C.; Cohen, R. E.; Hammond, P. T.; Rubner, M. F.; Wang, B. N. Industrial-Scale Spray Layer-by-Layer Assembly for Production of Biomimetic Photonic Systems. *Bioinspiration Biomimetics* **2013**, *8*, 045005.
39. Shukla, A.; Fang, J. C.; Puranam, S.; Jensen, F. R.; Hammond, P. T. Hemostatic Multilayer Coatings. *Adv. Mater.* **2012**, *24*, 492–496.
40. Andrews, D. A.; Low, P. S. Role of Red Blood Cells in Thrombosis. *Curr. Opin. Hematol.* **1999**, *6*, 76–82.
41. Monroe, D.; Hoffman, M.; Roberts, H. R. Platelets and Thrombin Generation. *Arterioscler., Thromb., Vasc. Biol.* **2002**, *22*, 1381–1389.
42. Cheng, T.-Y.; Wu, H.-C.; Huang, M.-Y.; Chang, W.-H.; Lee, C.-H.; Wang, T.-W. Self-Assembling Functionalized Nanopeptides for Immediate Hemostasis and Accelerative Liver Tissue Regeneration. *Nanoscale* **2013**, *5*, 2734–2744.
43. Rao, S. B.; Sharma, C. P. Use of Chitosan as a Biomaterial: Studies on Its Safety and Hemostatic Potential. *J. Biomed. Mater. Res.* **1997**, *34*, 21–28.
44. Klokkevold, P. R.; Fukayama, H.; Sung, E. C.; Bertolami, C. N. The Effect of Chitosan (Poly-N-Acetyl Glucosamine) on Lingual Hemostasis in Heparinized Rabbits. *J. Oral Maxillofac. Surg.* **1999**, *57*, 49–52.
45. Dowling, M. B.; Kumar, R.; Keibler, M. A.; Hess, J. R.; Bochicchio, G. V.; Raghavan, S. R. A Self-Assembling Hydrophobically Modified Chitosan Capable of Reversible Hemostatic Action. *Biomaterials* **2011**, *32*, 3351–3357.
46. Pusateri, A. E.; McCarthy, S. J.; Gregory, K. W.; Harris, R. A.; Cardenas, L.; McManus, A. T.; Goodwin, C. W., Jr. Effect of a Chitosan-Based Hemostatic Dressing on Blood Loss and Survival in a Model of Severe Venous Hemorrhage and Hepatic Injury in Swine. *J. Trauma* **2003**, *54*, 177–82.